Balanced Antipodal Vivaldi Antenna With Dielectric Director for Near-Field Microwave Imaging

Jeremie Bourqui, *Member, IEEE*, Michal Okoniewski, *Fellow, IEEE*, and Elise C. Fear, *Member, IEEE*

***Abstract*—A balanced antipodal Vivaldi antenna is designed to be used as a sensor for a microwave breast cancer detection system. The antenna has the ability to send short electromagnetic pulses into the near-field, with low distortion, low loss and in a directional manner. The antenna directivity is further improved by the inclusion of a novel feature in the antenna aperture called a "director" which consists of a profiled piece of higher dielectric constant material. Several simulated results are successfully confirmed with measurements. Reflections of a tumor placed in a breast model are simulated for two cases, namely a balanced antipodal Vivaldi antenna with and without a director. Greater tumor responses are recorded with the director present, demonstrating the potential of this feature for microwave breast imaging.**

***Index Terms*—Antenna, microwave breast imaging, radar, ultrawideband (UWB).**

I. Introduction

NEAR-FIELD microwave imaging approaches for exploring interior structures of the body are a topic of growing interest. For example, assessment of bone, heart and breast health with microwave techniques has been proposed [1]–[3]. One approach to biological microwave imaging is radar-based, which operates by sending a short-time pulse of microwaves towards the object of interest using one or many antennas. The reflections are measured and used to create an image related to the differences in dielectric properties of the structure. For breast imaging, recent studies indicate a wide range in dielectric properties of healthy tissues, which appears to be related to the content of adipose tissues [4]. A second study showed contrast between healthy and malignant tissues ranging from 1:10 to 10:11, depending on the adipose content [5]. In order to reliably sense the reflections from tumors located in tissues ranging from adipose to glandular, a high quality antenna is required to send and receive short-time microwave pulses with low distortion and high efficiency. Selective illumination of the breast may assist in tumor localization. Additionally, the antenna has to be compact in order to ease its placement around the breast and to be compatible with prototype imaging systems. This type of sensor is not commercially available.

Manuscript received January 14, 2009; revised July 15, 2009; accepted January 25, 2010. Date of publication April 22, 2010; date of current version July 08, 2010.

The authors are with the Department of Electrical and Computer Engineering, University of Calgary, Calgary, Alberta, AB T2N 1N4, Canada (e-mail: bourquij@ucalgary.ca).

Color versions of one or more of the figures in this paper are available online at http://ieeexplore.ieee.org.

Digital Object Identifier 10.1109/TAP.2010.2048844

Numerous antenna designs for radar-based ultrawideband (UWB) microwave breast imaging have been reported over the past decade. For example, stacked-patch [6] and wide slot [7] antennas have been developed at the University of Bristol. These antennas are mounted on a hemispherical surface and function as a multi-static system [8]. For monostatic data collection, a ridged pyramidal horn antenna [9] has been reported by the University of Wisconsin, and resistively loaded dipole, tapered slot, transverse electromagnetic horn, and balanced antipodal Vivaldi antennas have been presented by the University of Calgary (e.g., [10]). Our most recently developed antennas are designed to operate in an immersion medium of canola oil [11]. This immersion medium provides reduced antenna size and reflections from the skin when compared to free space, while providing reasonable imaging capabilities with an acceptable number of measurement locations. We further note that these antennas are designed to operate in, effectively, the radiative near-field.

The balanced antipodal Vivaldi antenna (BAVA) is a compact and versatile design that was introduced in [12]. We have modified the design for our near-field imaging application, as reported in [13]. The BAVA provides a more compact profile and lower reflections from the feeding structure than the tapered slot antenna [10]. In this paper, we introduce a significant improvement to our design which consists of a profiled dielectric piece with higher permittivity that is placed in the antenna aperture. We refer to this new feature as a "director" as it focuses the energy in the endfire direction in the near-field. We note that there is a body of work describing the addition of dielectric layers or radomes to tapered slot antennas (e.g., [14], [15]). These layers typically improve matching of compact elements and can result in increased antenna gain. This is a different concept from the director, in which the dielectric piece is included inside the aperture and effects changes in the radiation behavior without significant changes to the impedance. We also note that inclusion of materials with different dielectric properties in and around the aperture of tapered slotline antennas has been previously reported. For example, dielectric material is removed from the aperture of the antenna in order to provide a better match to free space in [16]. In [17], a dielectric rod is placed around the aperture of a Vivaldi antenna, acting as a second traveling wave antenna and resulting in improved gain and phase center stability. In both of these examples, the permittivity of the inclusion is lower than that of the antenna substrate. The director that we explore in this paper has a higher permittivity than the antenna substrate, does not improve the impedance matching of the antenna and is part of the radiation mechanism of the antenna itself. Hence this novel feature functions in a different manner than

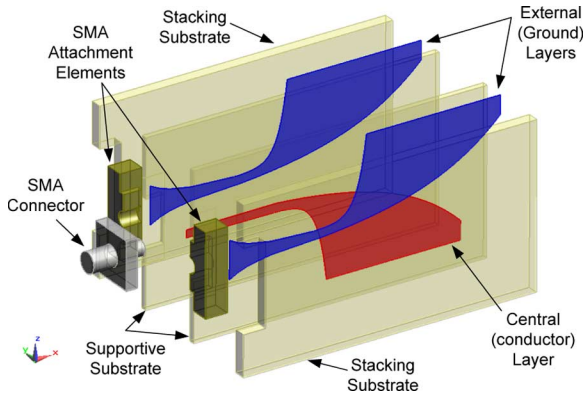

Fig. 1. Exploded view of the BAVA construction.

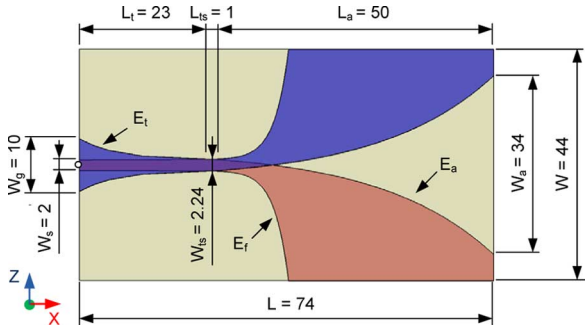

Fig. 2. Geometry and parameters of the BAVA copper pattern. The origin used to generate the curves is labeled as ∘.

previously reported work. In the context of microwave imaging application, a more focused beam illuminates a smaller volume which leads to an increase in the tumor-to-clutter ratio.

Section II introduces the BAVA design and the modified version including the dielectric director (BAVA-D). Section III presents the simulation and measurement methods used in this paper. Then, Section IV compares the BAVA and BAVA-D, with emphasis on the correlation between measured and simulated results and application to a breast model. The findings of the antenna studies are summarized in Section V.

II. Antenna Design

This section presents the BAVA design, then introduces the director and BAVA-D. Details on implementation of both designs are also provided.

A. BAVA

Our BAVA design follows concepts described in [12]. It consists of three copper layers; the two external layers are the ground planes and the central layer is the conductor (Fig. 1). The copper layers are separated by two dielectric substrates (supportive substrates) and two additional dielectric layers are stacked on each side of the antenna (stacking substrates). This novel feature balances the dielectric loading between the conductor and ground planes. As a result, the usual beam squint observed in this type of antenna construction [18] is considerably reduced. Moreover, for this application, the efficiency is improved since contact between the lossy canola oil and the external copper layers is avoided. The antenna is fed through an SMA connector followed by a gradual transition from a stripline to a tri-strip transmission line (TL). Along the transition, the conductor width increases linearly while the ground width decreases exponentially to keep constant impedance. The tri-strip TL extends for a short distance before the grounds and conductor start to flare in opposite directions with exponential curvatures to create the antenna aperture.

Fig. 2 presents the geometry and parameters values of the copper pattern. The curvatures E_t, E_f and E_a follow the exponential (1):

$$z = \pm A * e^{P(x-B)} + C \tag{1}$$

TABLE I
Curvatures Parameters and Relation to the Other Antenna Dimensions Dndicated in Fig. 2

Curves	Parameters			
	$A_{t,f,a}$	$P_{t,f,a}$	$B_{t,f,a}$	$C_{t,f,a}$
E_t	$\frac{W_{ts}-W_g}{2*(e^{P_t*L_t}-1)}$	-0.15	0	$\frac{W_g}{2}-A_t$
E_f	0.1	0.4	L_t+L_{ts}	$\frac{W_{ts}}{2}-A_f$
E_a	$\frac{W_{ts}-W_a}{2*(e^{P_a*L_a}-1)}$	0.05	L_t+L_{ts}	$-\frac{W_{ts}}{2}-A_a$

The curvatures parameters are listed in Table I. The overall antenna size is $80\times44\times9.2$ mm, including the SMA attachment elements length but excluding the SMA connector. We note that Fig. 2 does not include the SMA attachment elements length.

The antenna is constructed using RT/duroid 6002 (Rogers Corporation, CT, USA) which has a relative permittivity of 2.94. A photolithography process is used to pattern the copper and the bonding of the different layers is achieved using a thermoplastic Rogers 3001 bonding film ($\epsilon_r = 2.28$).

B. BAVA With Dielectric Director (BAVA-D)

The director consists of a shaped object of higher permittivity, placed in the aperture (Fig. 3). The director is expected to have two different effects. First, it should act as a waveguiding structure and direct most of the energy toward the aperture center. The second effect is related to the phase velocity, which will be lower in the director structure compared to the rest of the substrate. This produces differences in the propagation velocities in the director and the copper edges. As waves travel faster along the edges and the path length is physically longer, the overall effect is a more planar phase front near the aperture of the antenna (compared to the BAVA).

The shape of the director is designed to avoid reflections from its extremities, i.e., the start and the end of the aperture, shown respectively as A and B in Fig. 3 a. The section A approximately follows the aperture curves while the section B has been limited to a simple triangle that reasonably avoids reflections from the aperture. Fig. 3 shows the dimensions. The substrate length is extended by 4 mm compared to the original design to accommodate the director placement.

The BAVA-D is manufactured similarly to the BAVA. The opening in the substrate and the director are precisely machined using a milling machine and a water jet cutter respectively. The director is simply pressed into the opening and holds without

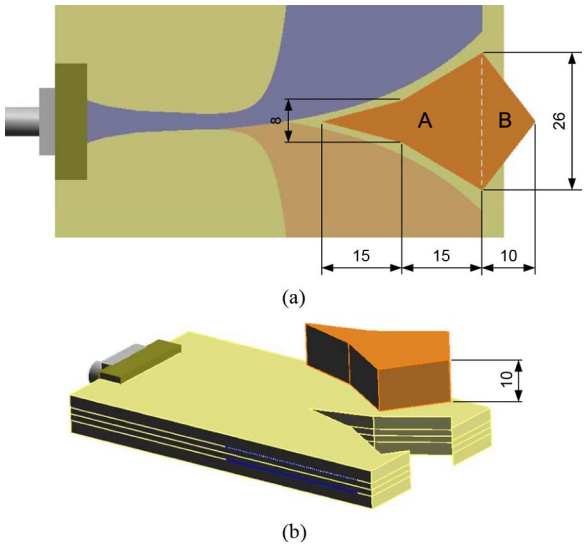

Fig. 3. BAVA including the higher dielectric permittivity director. (a) Top view and (b) 3D view with the director shown above its housing. For greater clarity the dielectric layers are shown as transparent in (a). All dimensions are in mm.

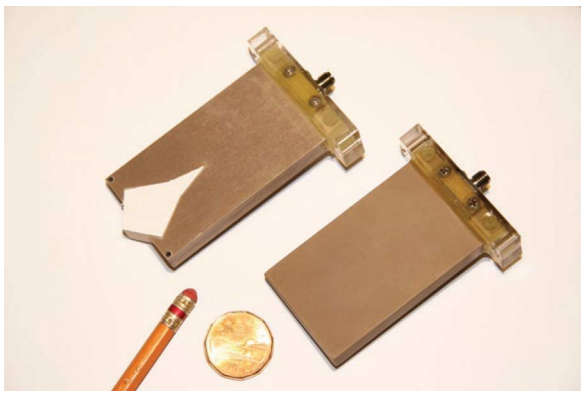

Fig. 4. The constructed BAVA (right) and BAVA-D (left).

any adhesive. The director is made of Eccostock HIK material (Emerson & Cuming Microwave Product, MA, USA) with relative permittivity of 6. This permittivity has been selected since it produces the expected effect, however other values may be utilized. The constructed antennas with and without the director are shown in Fig. 4.

III. Evaluation Methods

In order to test the BAVA and BAVA-D, full wave simulations are performed. In addition to reflection and transmission, several near-field parameters are introduced for antenna performance assessment. The manufactured antennas are immersed in oil, and measurements are collected in order to compare simulated and measured data.

A. Simulation

Simulated results are obtained using SEMCAD X (SPEAG, Zurich, Switzerland), which utilizes the finite-difference time-domain (FDTD) technique. To feed the antenna, a coaxial transmission line is connected to the stripline and represents the SMA-stripline transition used in practice. The coaxial line is excited using a waveguide source. The mesh size is 1/14 of the smallest wavelength or smaller where refinements are needed due to geometrical features of the antenna. Perfectly matched layers (PML) are used for boundary conditions.

Our microwave imaging system utilizes canola oil as an ambient immersion medium, so canola's electrical properties are assigned to the background of each simulation. From 1 to 14 GHz, its permittivity and conductivity vary from approximately 2.55 to 2.35 and 0.01 to 0.04 S/m, respectively, [19]. For most simulations, it was found sufficient to consider an average relative permittivity value of $\epsilon_r = 2.5$ and the maximum conductivity of $\sigma = 0.04\ \mathrm{S/m}$. However, in some cases, such as comparing simulations with measurements, a single pole Debye model may be used to represent the property variations with frequency

$$\tilde{\epsilon_r}(\omega) = \epsilon_{r\infty} + \frac{(\epsilon_{r\,static} - \epsilon_{r\infty})}{1 + j\omega\tau} + \frac{\sigma_s}{j\omega\epsilon_0} \tag{2}$$

where $\tilde{\epsilon_r}$, is the complex relative permittivity, $\omega = 2\pi f$ denotes the angular frequency, $\epsilon_{r\,static} = 2.514$ is the static relative permittivity, $\epsilon_{r\infty} = 2.28$ is the relative permittivity at infinity, $\tau = 27.84$ ps is the relaxation time and $\sigma_s = 0.008\ \mathrm{S/m}$ is the static conductivity.

The performance of the antennas is evaluated in terms of: S_{11}, S_{21}, half energy beamwidth (HEBW), half energy beam (HEB) and fidelity. S_{11} and S_{21} are simulated using the standard broadband excitation implemented by SEMCAD X, however the simulations for the HEBW, HEB and fidelity are computed using a specific ultrawideband pulse [20] of the form:

$$V(t) = V_0 \cdot (t - t_0) \cdot e^{-(t-t_0)^2/\tau^2} \tag{3}$$

where V_0 is used to adjust the amplitude of the pulse, $\tau = 62.5$ ps and $t_0 = 4\tau$. This pulse contains energy, above 10% of its maximum, from 20 MHz to 10 GHz in the frequency spectrum.

The HEBW and HEB are based on the energy radiated by the antenna. The energy in and around the antenna structure is calculated by summing time samples of the instantaneous Poynting vector over the duration of the simulation time. We term this quantity the energy flux density (EFD).

In the near-field, we define the HEBW on a plane orthogonal to the main radiation beam and situated at a given distance from the antenna aperture. The HEBW describes the region over which the energy is greater than half of the maximum value on the selected plane. For the example shown in Fig. 5(a), the antenna is aligned with the x-axis, so the HEBW is evaluated in the y- and z-directions. The HEB attempts to provide a more general representation of the radiation beam in the near-field. Fig. 5(b) shows the HEBW calculated along the x-axis instead of at a single point as shown by Fig. 5(a). To provide a more general representation of the radiation beam in the near-field, we model the conical shape with an equivalent angle in conjunction with a corresponding beam origin. As shown in Fig. 5(b), the HEB angle and origin are defined by fitting the half energy contour and maximum energy path recorded on a series of planes to linear functions. The HEB representation in the near-field

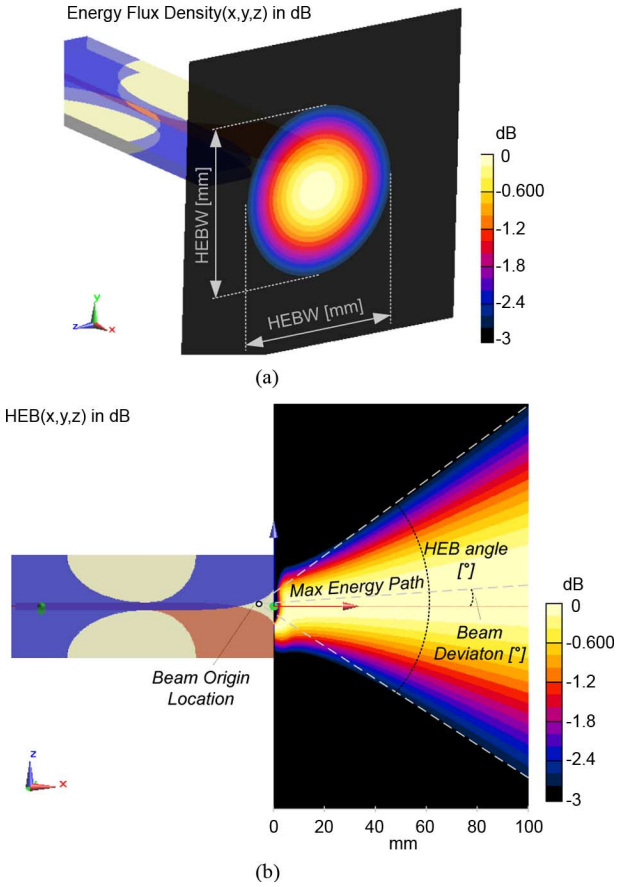

Fig. 5. Half energy area on one plane (a) and HEB representation (b).

is powerful since, by including the beam origin information, it models the radiation behavior as function of the actual antenna structure and size. This makes radiation pattern comparison between antennas more straightforward and makes prediction of the radiation coverage of an object placed close to the antenna possible.

The fidelity measures how faithfully the excitation pulse is transmitted or received by the antenna and therefore reflects the distortion due to the frequency band limitation and phase non-linearity [21]. Only the transmitting fidelity is of interest. It is calculated using the main polarization component (z component) of the electric field and the first derivative of the excitation pulse is used as a reference signal. The maximum value of fidelity is one.

B. Measurement

All of the measurements are obtained with the antennas immersed in canola oil and data are recorded by an Agilent 8719ES Vector Network Analyzer (VNA) (Agilent, Palo Alto, CA). The time signals are synthetically created from the frequency domain S parameters. First, a Chirp-Z transform is used to find the frequency-domain representation of (3) at the measured frequencies. Next, the measured S-parameters are multiplied with the frequency-domain version of the excitation. Finally, the inverse Chirp-Z transform is used to obtain the time-domain signals [22].

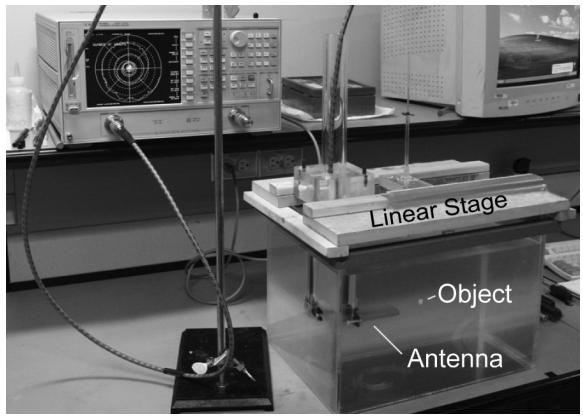

Fig. 6. Measurement setup including the VNA, oil tank, positioning system, antenna and one of the objects used to record reflections.

Reflections are measured from objects consisting of cubes and spheres of dimensions varying from 13 mm to 3.2 mm. The objects are made out of Eccostock HIK and TMM6 (Rogers Corporation) materials with relative permittivities of 10 and 6, respectively. These objects are attached to a Plexiglas rod ($\epsilon_r = 2.6$) and positioned in front of the antenna using a manual linear stage as shown in Fig. 6. In order to extract the reflections from the objects, a reference measurement of the Plexiglas rod is subtracted from the total measurement. The resulting signal is referred to as the calibrated response. S_{21} is measured using the same setup but with two antennas facing each other and separated by a known distance.

The near-field radiation pattern is measured using a dosimetric assessment system (DASY 4 Professional, SPEAG). The antenna is placed in the same tank of oil as presented in Fig. 6. The radiated E-field is measured at 2.45, 4, 5.1, 5.9 GHz. Only relative radiation intensity is measured since the probes are not calibrated for canola oil.

IV. Results

The director influence is assessed by comparing the BAVA-D performance to the original BAVA design with simulated and measured results. S-parameters, radiation fields, backscatter reflections and ability to sense a tumor in a breast model are presented.

A. S-Parameters

The simulated reflection coefficients (S_{11}) of the original BAVA and the BAVA-D are shown in Fig. 7. Both antennas operate over a 2.4 to 18 GHz band and no substantial difference is observed between the two versions besides slightly higher reflections at lower frequencies for the BAVA-D.

In Fig. 8, the measured S_{11} of two constructed BAVA-Ds are compared with the simulated data. The measurements match the main trends of the simulations. The main source of error comes from the thermoplastic used to bond the different layers together, since it does not match the substrate permittivity ($\epsilon_r = 2.28$ compared to 2.94 for the substrate). However, the measured

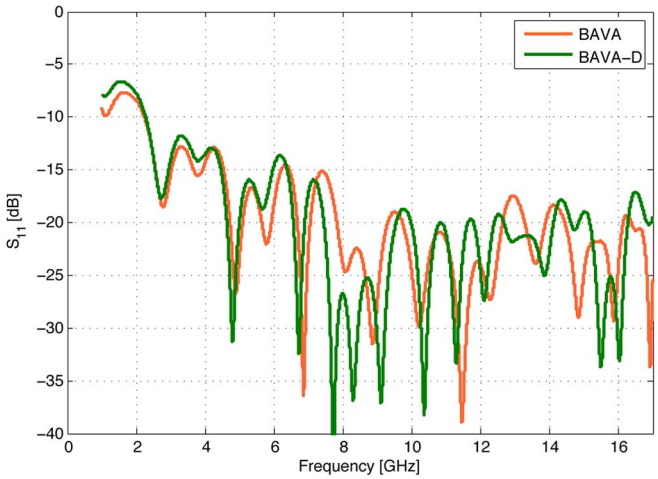

Fig. 7. Simulated S_{11} for the BAVA and BAVA-D.

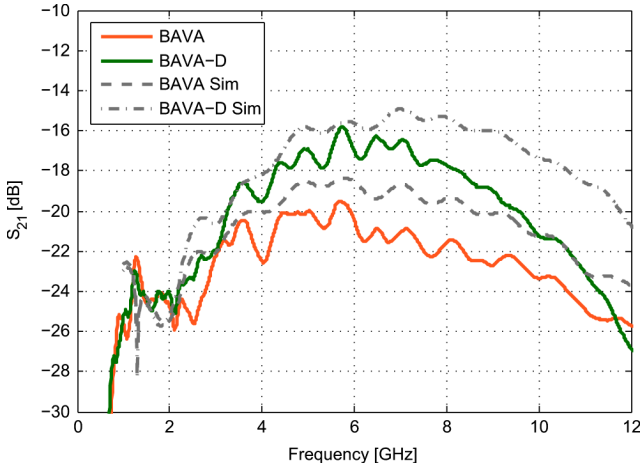

Fig. 9. Transmission coefficient (S_{21}) obtained with two antennas facing each other with 100 mm separation (metalization end as reference).

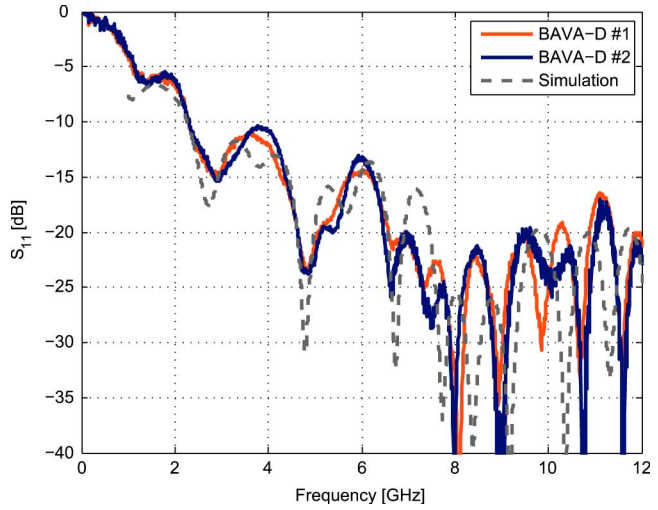

Fig. 8. Measured BAVA-Ds S_{11} compared to the simulation data.

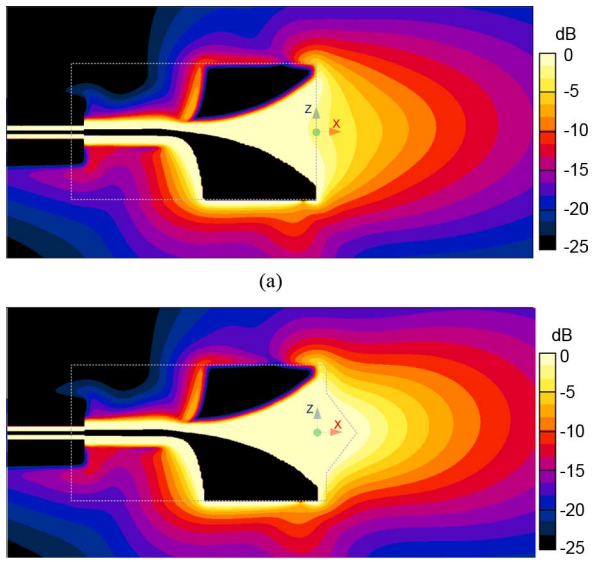

Fig. 10. Simulated total EFD on the Y plane @ $y = 0$ for the (a) BAVA and (b) BAVA-D. Data are normalized by the input energy. The EFD at each point is the sum of the sampled instantaneous Poynting vector over the duration of the simulation.

results remain acceptable since the bandwidth is not significantly altered. Similar agreement is seen with the BAVA [13].

Next, the transmission parameter (S_{21}) between two antennas assesses the improvements due to the director in the frequency domain. From a detection perspective, an antenna with higher S_{21} will receive more reflected energy from an object placed in front of the antenna. Fig. 9 presents the simulated and measured S_{21} for both antennas facing each other and separated by 100 mm (metalization end as reference). First, it is observed that the director increases the S_{21} magnitude between 2 to around 12 GHz. Similar behavior has been observed at separation distances between 40 to 150 mm and therefore it is concluded that there is no direct dependence on the separation distance. Second, it is observed that the measured data does not match the magnitude of the simulated results for both antennas. This discrepancy mostly stems from the canola oil. When the same scenario is reproduced in the air, a good match is found between simulated and measured results. The reason for the disagreement, when the antennas are immersed in canola oil, is unknown and is being investigated. Nevertheless, S_{21} measurements exhibit the same trends as the simulations and it can be observed that the transmitted power is increased by approximately the same ratio when the director is present.

B. Radiated Fields

To define the beamwidth, the EFD is computed on Y and Z planes ranging from the antenna feed point to a distance of 70 mm away from the aperture. These data are shown for both antennas in Fig. 10 for the Y plane. The endfire radiation behavior is evident, while it can be noticed that the director significantly increases the near-field directivity of the BAVA. A slight increase in the back radiation is noticed when the director is present, however the front to back ratio is still 35% higher compared with the original BAVA. When the radiation behavior is analyzed in the frequency domain, it is observed that the director effect increases with frequency. This phenomenon is confirmed by the transmission coefficient in Fig. 9 while Fig. 11

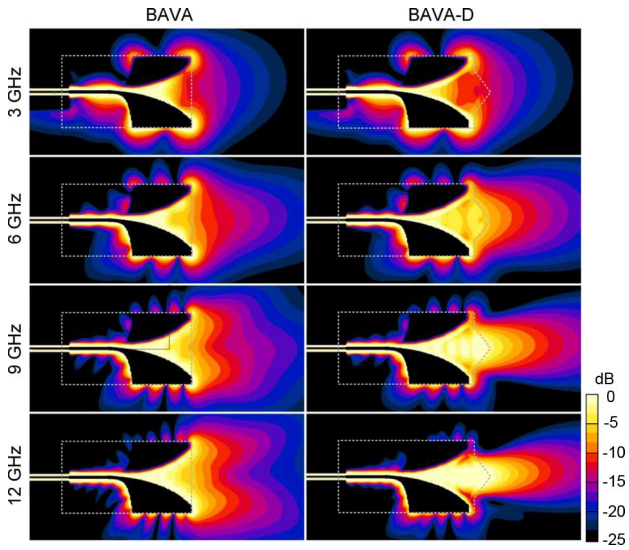

Fig. 11. Simulated radiated E-field RMS modulus at 3, 6, 9 and 12 GHz on the Y plane @ $y = 0$ for the BAVA and BAVA-D. The fields are normalized in proportion to the energy accepted by each antenna at each frequency.

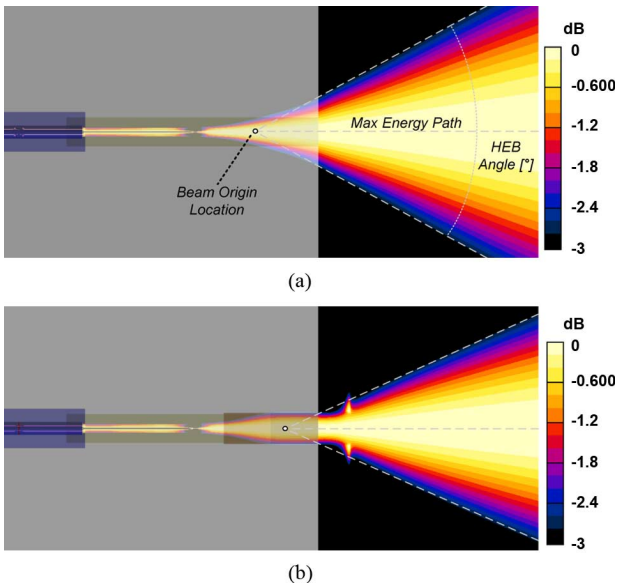

Fig. 12. Simulated HEB on the Z plane for the (a) BAVA and (b) BAVA-D. Dotted lines represent the half energy limits and the maximum energy path with the beam origin indicated by the circle.

illustrates this effect at selected frequencies. The HEB view in the Z plane (Fig. 12) shows that, when the director is present, the pulse energy stays concentrated inside the antenna structure while it starts to expand outside the substrate boundary around 15 mm before the end of the antenna for the original design. This illustrates the waveguide effect produced by the director.

A quantitative comparison of the beamwidth is contained in Table II. As expected the effect of the director on the beamwidth is an overall narrowing on both axes as demonstrated by the HEBW values at 20 and 50 mm. It is observed that the director improvement to beamwidths in the Y and Z planes is not necessarily due to a smaller HEB angle as a shift of the beam origin towards the antenna aperture occurs. For example the HEB angle on the Y plane actually increases from 32° to 34° however the

TABLE II
SIMULATED BEAMWIDTH RESULTS FOR THE BAVA AND BAVA-D

Parameters	Y plane		Z plane		Unit
	BAVA	BAVA-D	BAVA	BAVA-D	
HEB angle	32	34	60	51	°
Beam Deviation	3	4	0	0	°
Beam Origin	x = -28 z = -2	x = -15 z = -1.3	x = -17 y = 0	x = -8 y = 0	mm
HEBW @20mm	34	23	45	42	mm
HEBW @50mm	44	40	80	58	mm

HEBW measured at 20 and 50 mm are smaller with the director present. This occurs because the energy starts to expand further along the antenna in the X direction which is clearly expressed by the shift of the beam origin from $x = -28$ mm to $x = -15$ mm with the director (Table II). On the Z plane, the director actually reduces the HEB angle from 60° to 51° while the beam origin is also moved from $x = -17$ mm to $x = -8$ mm. Therefore the HEBW on the Z plane is significantly reduced as indicated in Table II. For the BAVA and BAVA-D, beam deviations of 3° and 4°, respectively, appear on the Y plane while no deviation is observed on the Z plane. Thus the director slightly increases the beam deviation on the Y plane.

Next, the measured radiation pattern in the near-field is compared with simulation. Very good agreement is found for both antennas at all tested frequencies. A typical result is shown in Fig. 13 for the BAVA-D at 5.1 GHz.

The simulated fidelity is very close to 1 for both antennas, with values above 0.9 at the aperture and above 0.96 from 20 mm away, as shown by Fig. 14. For the original BAVA, the fidelity logically increases with the distance from the aperture, however the version with the director has a higher fidelity closer to the antenna which slightly decreases further away. This behavior is a direct effect of the director which evenly concentrates the radiated energy, across the frequency band, closer to the antenna aperture. The fidelity of the radiated pulse has not been measured because of equipment limitations. However the following section shows correlation between measured and simulated reflections from different objects, supporting the fidelity results.

C. Backscatter Reflections

Reflections from different objects placed 40 mm in front of the antenna aperture are measured and compared with simulated data. The dispersive behavior of the canola oil is included in simulations to closely reproduce the measurement environment. To calibrate the simulated data, the response computed without an object is subtracted from the total response received with the object present. To facilitate comparison between measured and simulated data, each signal is normalized to its maximum absolute value. Additionally the simulated signal is slightly shifted to be aligned with the measured data. Representative instances of the reflected signals are shown in Fig. 15 which illustrates the reflections from a $6 \times 6 \times 6$ mm cube made of Eccostock HIK $= 10$ material ($\epsilon_r = 10$). The shapes of measured backscatter signals are consistent with their simulated counterparts for both antennas. The good correlation between measured

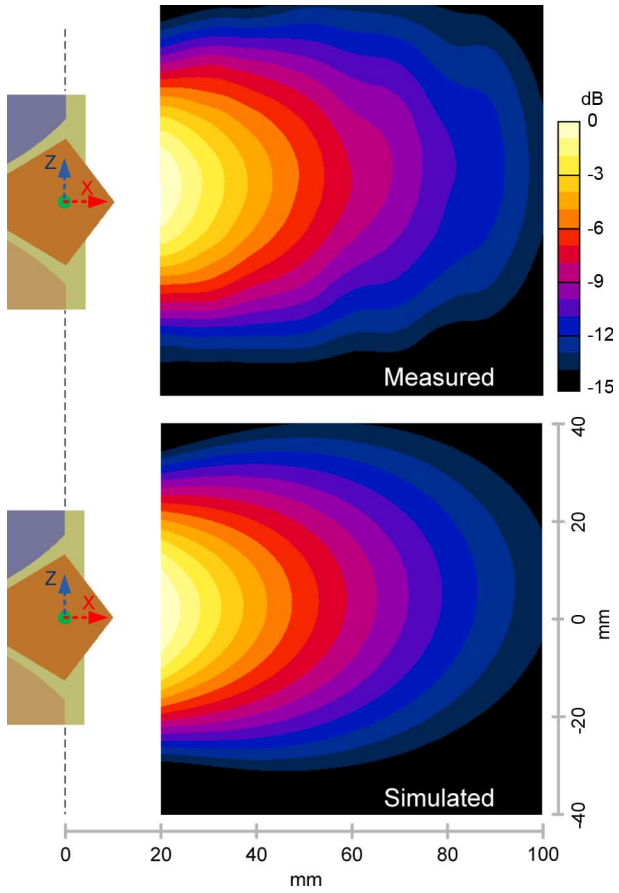

Fig. 13. Simulated and measured radiation pattern at 5.1 GHz for the BAVA-D.

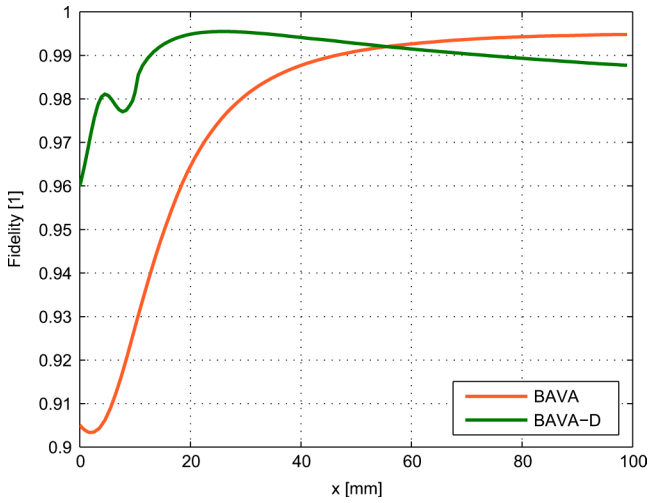

Fig. 14. Simulated fidelity along an X-directed line away from the antenna aperture. (x = 0 at the aperture as in Fig. 13).

and simulated signatures supports the simulated fidelity results presented earlier.

Next, the intensity of the backscatter signal is explored. The simulated results obtained for the different objects demonstrate an increase in reflected intensity ranging from 2.6 to 3.6 when the director is used. It is also observed that smaller objects tend to increase this ratio, which makes sense since a narrower beam would increase the illumination of a small surface compared

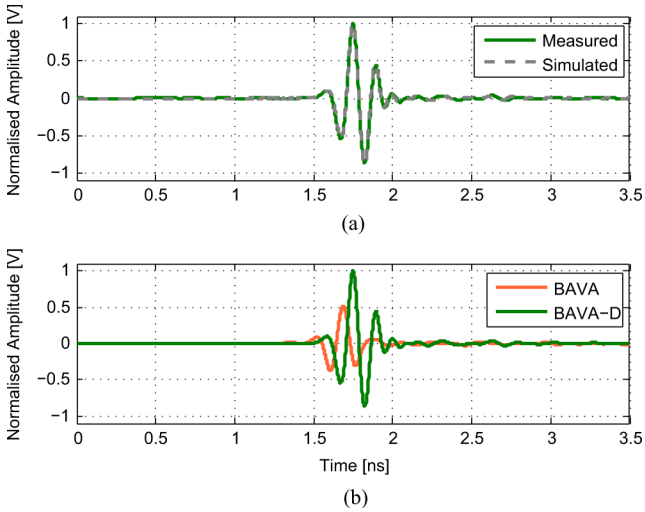

Fig. 15. Calibrated Backscatter time domain signature produced by a $6 \times 6 \times 6$ mm cube made of Eccostock HIK $= 10$ material ($\epsilon_r = 10$). (a) Measured vs simulated time signature using the BAVA-D. (b) Measured reflected signal using the BAVA and BAVA-D.

to a large one. The measurements (Fig. 15(b)) confirm the increase in reflected energy observed with the director and its dependence on the object size. The BAVA-D tends to have slightly stronger late time ringing compared to the BAVA. This behavior is not surprising and improvement in this ringing may be expected with a modified director shape.

D. Tumor Detection in Realistic Breast Model

Since the ultimate purpose of these antennas is to sense breast tumors, simulations have been performed to assess the improvement induced by the director for this particular application. For this task, a breast model of realistic shape, derived from an MRI scan, is imported into SEMCAD X. The simulation model is presented in Fig. 16. A 40 mm thick object, that replicates the chest wall, is added on the upper part of the breast model. The breast interior is homogeneous and is simulated as adipose tissue. A 6 mm tumor is placed at a distance of 30 mm from the skin. The electric properties of breast tissues at microwave frequencies are modeled in SEMCAD X using single pole Debye models. The Debye parameters presented in [23] are used for the adipose tissue and tumor while the data measured in [24] are used to simulate dry skin. The chest wall, with a relative permittivity of 50 and electrical conductivity of 4 S/m, is not modeled as a dispersive material. The parameters for the different Debye models can be found in Table III.

The antenna is aligned with the tumor and placed approximately 20 mm from the breast surface. The antenna scans the model in a circular pattern with 18 degree increments. The zero degree (reference) location is defined in Fig. 17. For each position, simulations are performed with and without the tumor present, such that the tumor reflections can be extracted from the overall signal by a simple subtraction. The energy contained in the tumor reflection at each antenna position is calculated and normalized to the maximum reflected energy sensed by the BAVA.

Fig. 17 presents the EFD in the coronal plane of the breast models with the antennas at the reference location. It is observed

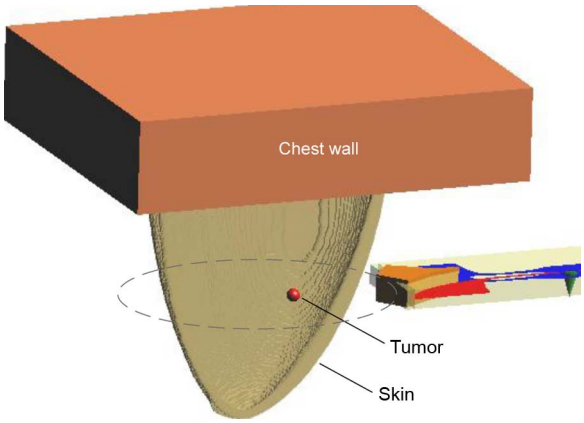

Fig. 16. The breast model including the tumor and the antenna. The skin and the interior of the breast are transparent to show the tumor.

TABLE III
DEBYE PARAMETERS USED TO MODEL THE PROPERTIES OF THE DIFFERENT BREAST TISSUES

Parameter	Dry Skin	Adipose Tissue (group 3)	Tumor	Unit
$\epsilon_{r\,static}$	37	4.74	54.66	
$\epsilon_{r\,\infty}$	4	3.14	6.75	
σ_{disp}	1.1	0.036	0.79	S/m
τ	7.23	13.56	10.1	ps

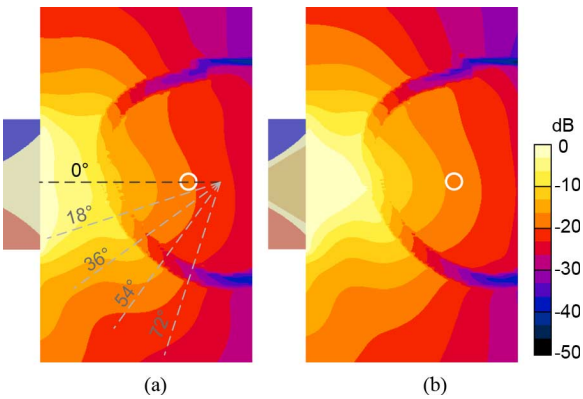

Fig. 17. Total EFD on the Y plane, radiated by (a) the BAVA and (b) BAVA-D inside the breast. The circle represents the tumor location. Data are normalized by the input energy.

that more energy penetrates into the breast when the director is used. Fig. 18 demonstrates that this increase is also noted as the antenna is scanned around the breast. Specifically the BAVA-D magnifies the tumor reflection by 3 to 4 dB for all positions. For this specific scenario, the reduced beamwidth does not reduce the number of locations at which the tumor is sensed. Practically, the number of locations at which the tumor response is received relates to the breast size, tumor location and glandular tissue distribution. The decrease in beamwidth may result in a small increase in the number of scan locations; however this is

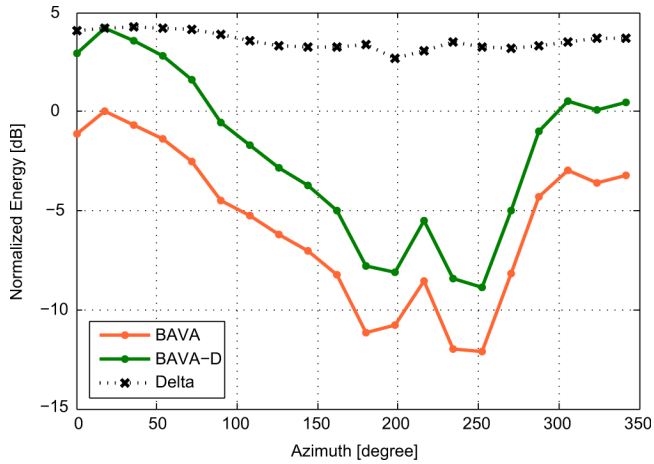

Fig. 18. Energy reflected by the tumor sensed with the BAVA and BAVA-D in function of azimuth position. The values are normalized to the maximum energy sensed by the BAVA. The delta values correspond to the difference between the BAVA-D and BAVA energies.

compensated for in practical terms by the increased tumor response.

V. CONCLUSION

In this paper the near-field directivity of a BAVA is improved by the inclusion of higher permittivity and specially shaped material in the aperture. This novel feature is called the director. The BAVA-D produces a narrower beamwidth and generally higher fidelity while keeping S_{11} below -10 dB between 2.4 to 18 GHz (SMA connector limit).

The effect of this narrower beamwidth is also noticed in S_{21} since the transmitted energy between two antennas is significantly higher when the director is present. Additionally, it is demonstrated that the BAVA-D increases the backscatter energy from an object placed in front of the antenna, such as a tumor contained in a breast. From a detection point of view, this is an advantage. Only basic explanations about the physical effect of the director are given in this paper. A deeper analysis of the director effect and the influence of its permittivity, shape and size is ongoing.

Finally, we note that the director is expected to produce similar effect when applied to any type of aperture-based traveling wave antenna.

ACKNOWLEDGMENT

The authors would like to acknowledge the technical support of F. Hickli, B. Isenor, C. Stern, R. Scorey, T. Williams and J. Shelley, all of the University of Calgary, Calgary, AB, Canada.

REFERENCES

[1] S. Semenov, V. Posukh, A. Bulyshev, and T. Williams, "Microwave tomographic imaging of the heart in intact swine," *J. Electromagn. Waves Applicat.*, vol. 20, no. 7, pp. 873–890, 2006.

[2] S. Semenov *et al.*, "Microwave tomography for functional imaging of extremity soft tissues: Feasibility assessment," *Phys. Med. Biol.*, vol. 52, no. 18, pp. 5705–5719, 2007.

[3] T. Rubaek, P. Meincke, and O. Kim, "Three-dimensional microwave imaging for breast-cancer detection using the log-phase formulation," in *Proc. IEEE Antennas Propag. Soc. Int. Symp.*, 2007, pp. 2184–2187.
[4] M. L. Lazebnik *et al.*, "A large-scale study of the ultrawideband microwave dielectric properties of normal breast tissue obtained from reduction surgeries," *Phys. Med. Biol.*, vol. 52, no. 10, pp. 2637–2656, May 2007.
[5] M. L. Lazebnik *et al.*, "A large-scale study of the ultrawideband microwave dielectric properties of normal, benign and malignant breast tissues obtained from cancer surgeries," *Phys. Med. Biol.*, vol. 52, no. 20, pp. 6093–6115, Oct. 2007.
[6] R. Nilavalan, I. Craddock, J. Leendertz, A. Preece, and R. Benjamin, "Wideband microstrip patch antenna design for breast cancer tumour detection," *IET Microwaves Antennas Propag.*, vol. 1, pp. 277–281, 2007.
[7] D. R. Gibbins, M. Klemm, I. Craddock, G. Hilton, and D. Paul, "The design of a wide slot antenna for the transmission of UWB signals into the human body using FDTD simulation," in *Proc. 2nd Eur. Conf. Antennas Propag.*, Edinburgh, U.K., Nov. 11–16, 2007, vol. 1, 5 pages.
[8] I. Craddock, M. Klemm, J. Leendertz, A. Preece, and R. Benjamin, "An improved hemispherical antenna array design for breast imaging," in *Proc. 2nd Eur. Conf. Antennas Propag.*, Edinburgh, U.K., Nov. 11–16, 2007, 5 pages.
[9] X. Li, S. Hagness, M. Choi, and D. van der Weide, "Numerical and experimental investigation of an ultrawideband ridged pyramidal horn antenna with curved launching plane for pulse radiation," *IEEE Antennas Wireless Propag. Lett.*, vol. 2, pp. 259–262, 2003.
[10] J. Bourqui, M. A. Campbell, J. Sill, M. Shenouda, and E. C. Fear, "Investigation of antenna performance for ultra-wideband microwave breast imaging," in *Proc. IEEE Radio Wireless Symp.*, San Diego, CA, 2009, pp. 522–525.
[11] J. Sill and E. Fear, "Tissue sensing adaptive radar for breast cancer detection: Study of immersion liquids," *Electron. Lett.*, vol. 41, no. 3, pp. 113–115, 2005.
[12] J. Langley, P. Hall, and P. Newham, "Novel ultrawide-bandwidth Vivaldi antenna with low crosspolarisation," *Electron. Lett.*, vol. 29, no. 23, pp. 2004–2005, 1993.
[13] J. Bourqui, M. Okoniewski, and E. C. Fear, "Balanced antipodal Vivaldi antenna for breast cancer detection," in *Proc. 2nd Eur. Conf. Antennas Propag.*, Edinburgh, U.K., Nov. 11–16, 2007, 5 pages.
[14] R. Simons and R. Lee, "Impedance matching of tapered slot antenna using a dielectric transformer," *Electron. Lett.*, vol. 34, no. 24, pp. 2287–2289, 1998.
[15] D. Schaubert, S. Kasturi, A. Boryssenko, and W. Elsallal, "Vivaldi antenna arrays for wide bandwidth and electronic scanning," in *Proc. 2nd Eur. Conf. Antennas Propag.*, Edinburgh, U.K., Nov. 11–16, 2007, 6 pages.
[16] N. Schuneman, J. Irion, and R. Hodges, "Decade bandwidth tapered notch antenna array element," in *Proc. Antenna Applicat. Symp.*, 2001, pp. 280–294.
[17] A. Elsherbini, C. Zhang, S. Lin, M. Kuhn, A. Kamel, A. Fathy, and H. Elhennawy, "Uwb antipodal Vivaldi antennas with protruded dielectric rods for higher gain, symmetric patterns and minimal phase center variations," in *Proc. IEEE Antennas Propag. Soc. Int. Symp.*, 2007, pp. 1973–1976.
[18] J. Langley, P. Hall, and P. Newham, "Balanced antipodal Vivaldi antenna for wide bandwidth phased arrays," *Proc. Inst. Elect. Eng. Microwaves Antennas Propagat.*, vol. 143, no. 2, pp. 97–102, 1996.
[19] J. M. Sill, "Second generation experimental system for tissue sensing adaptive radar," Master's thesis, Dept. Elect. Comput. Eng., Schulich School of Engineering, University of Calgary, Calgary, AB, Canada, 2005.
[20] E. Fear, X. Li, S. Hagness, and M. Stuchly, "Confocal microwave imaging for breast cancer detection: Localization of tumors in three dimensions," *IEEE Trans. Biomed. Eng.*, vol. 49, pp. 812–822, 2002.
[21] T. Montoya, T. Montoya, and G. Smith, "A study of pulse radiation from several broad-band loaded monopoles," *IEEE Trans. Antennas Propag.*, vol. 44, no. 8, pp. 1172–1182, 1996.
[22] B. Ulriksson, "Conversion of frequency-domain data to the time domain," *Proc. IEEE*, vol. 74, pp. 74–77, Jan. 1986.
[23] M. Lazebnik, M. Okoniewski, J. Booske, and S. Hagness, "Highly accurate Debye models for normal and malignant breast tissue dielectric properties at microwave frequencies," *IEEE Microw. Wireless Compon. Lett.*, vol. 17, no. 12, pp. 822–824, 2007.
[24] D. W. Winters, E. J. Bond, B. D. Van Veen, and S. C. Hagness, "Estimation of the frequency-dependent average dielectric properties of breast tissue using a time-domain inverse scattering technique," *IEEE Trans. Antennas Propag.*, vol. 54, no. 11, pp. 3517–3528, 2006.

Jeremie Bourqui was born in Switzerland in 1982. He received the Ing. HES (B.Sc.) degree in electrical engineering from the University of Applied Sciences, Fribourg, Switzerland, in 2004 and the M.Sc. degree from the University of Calgary, Calgary, AB, Canada, in 2008.

He is currently a Research Engineer at the University of Calgary. His work involves the design, implementation and testing of a microwave breast imaging system. This includes UWB sensors, RF measurement and antenna positioning systems.

Michal Okoniewski (F'09) is a Professor in the Department of Electrical and Computer Engineering, University of Calgary, Calgary, AB, Canada, where he holds the Libin/Ingenuity Chair in biomedical-engineering and Canada Research Chair in Applied Electromagnetics. His interests range from computational electrodynamics, to tunable reflectarrays, RF MEMS and RF micro-machined devices, as well as hardware acceleration of computational methods. He is also involved in bio-electromagnetics, where he works on tissue spectroscopy and micro-imaging. In 2004 he cofounded Acceleware Corp.

Elise C. Fear (S'98–M'02) received the Ph.D. degree in electrical engineering from the University of Victoria, Victoria, BC, Canada, in 2001.

She was an NSERC (Natural Sciences and Engineering Research Council of Canada) Postdoctoral Fellow in electrical engineering at the University of Calgary, Calgary, AB, Canada from 2001 to 2002, and is currently an Associate Professor in the same department. Her research interests include microwave breast cancer detection.

Dr. Fear is currently serving as an Associate Editor for the IEEE TRANSACTIONS ON BIOMEDICAL ENGINEERING, and was awarded the 2007 Outstanding Paper Award from the same journal.